Postprint of: Rycewicz M., Ficek M., Gajewski K., Kunuku S., Karczewski J., Gotszalk T., Wlasny I., Wysmołek A., Bogdanowicz R., Low-strain sensor based on the flexible boron-doped diamond-polymer structures, CARBON, Vol. 173 (2021), pp. 832-841, DOI:10.1016/j.carbon.2020.11.071

# Low-strain Sensor Based on the Flexible Boron-Doped Diamond-Polymer Structures

*M. Rycewicz[1], M. Ficek[1*], K. Gajewski[2], S. Kunuku[1], J. Karczewski[3], T. Gotszalk[2], I. Wlasny[4], A.Wysmolek[4], R. Bogdanowicz[1*]*

[1] *Department of Metrology and Optoelectronics, Faculty of Electronics, Telecommunications and Informatics, Gdańsk University of Technology, 11/12 Narutowicza St., 80-233 Gdańsk Poland*

[2] *Department of Nanometrology, Wrocław University of Science and Technology, Janiszewskiego 11/17 St., 50-372 Wrocław, Poland*

[3] *Department of Solid State Physics, Faculty of Applied Physics and Mathematics, Gdańsk University of Technology, 11/12 Narutowicza St., 80-233 Gdańsk Poland*

[4] *Institute of Experimental Physics, Faculty of Physics, University of Warsaw, Pasteura 5 St., 02-093 Warsaw, Poland*

* Corresponding author: e-mail: *matficek@pg.edu.pl*, *+48 3471503 (M. Ficek)*

**Abstract:** A free-standing high boron-doped diamond nanosheet (BDDNS) has been fabricated for the development of a flexible BDDNS strain senor. A high boron-doped diamond was initially grown on a tantalum substrate in a microwave plasma-assisted chemical vapor deposition method, and was then transferred to a Kapton polymer substrate to fabricate the flexible BDDNS/Kapton device. Before performing the transfer process, the thin BDDNS's morphology and bonding structure on the top and bottom sides were investigated using scanning electron microscopy and Raman spectroscopy. The contact potential difference and work function values of the BDDNS top and bottom surfaces were measured using a Kelvin probe atomic force microscope. Significant electrical conducting properties were observed from the resistance mapping of the BDDNS foil, and the average resistance value of 31 Ω attained from the top-surface of the BDDNS foil. The electrical response of the BDDNS/Kapton device was investigated using a custom-made device and a positive residual resistance change with strain was observed. The developed BDDNS/Kapton device was able to sustain for measuring up to 0.55 % of strain, which indicates it may have great potential to be utilized in low-strain sensor applications.

## 1. Introduction

Diamond is considered as one of the hardest minerals on earth due to its exceptional mechanical durability, as a result of its $sp^3$ hybridization and tetrahedral shape [1]. Besides this, diamond shows some exceptional properties, including high thermal conductivity [2] and low absorption in visible light, because of its high optical band gap (E = 5.48 eV) [3]. The refractive index of an undoped diamond is 2.418 [1], although doping with suitable elements is able to modify the refractive index of diamond as well as its conductivity. In general, the common route to attain p- and n-type semiconducting properties in a diamond is to dope it with boron or phosphorus, respectively. It should be noted that the semiconducting diamond is characterized by high electron and hole mobilities of >2000 $cm^2/(Vs)$ [4] and P-type diamond is particularly desirable in chemistry, due to its wide potential window and low background currents [5]. As mention above, P-type diamond can be synthesized by boron doping into diamond, and boron requires a low activation energy (0.37 eV) in comparison with other dopant elements [6].

One of the primary factors that affects the conductivity of a diamond and the shape of the Raman spectra is the size of the diamond grains. May et al. reported that boron-doped diamond with large grains exhibited higher conductance than those with smaller crystalline sizes for the same boron doping [7]. Therefore, the conductance of boron-doped microcrystalline diamond films was much higher than for nanocrystalline diamond films. Gajewski et al. investigated the conductivity of thin diamond films (<350 nm) deposited on a quartz substrate, where the heavily boron-doped films ($3.3 \times 10^{21}$ $cm^{-3}$) were shown to have a conductivity of 76 $\Omega^{-1}$ $cm^{-1}$, and a significant effect of temperature on the resistivity of the low-born doped samples was observed [8]. In the case of transparent boron-doped nanodiamond layers with a thickness of 150 nm, Zuerbig et al. reported a conductivity of 50–60 $\Omega^{-1}$ $cm^{-1}$ for diamond films with a boron concentration up to $10^{21}$ $cm^{-3}$ [9]. The other factors that can improve the conductivity of nanodiamond layers are surface hydrogenation, which increases the conductivity by two orders of magnitude [10], and the presence of the right amount of the $sp^2$ phase [11]. Ma et al. suggested that the functionalization of chemically inert diamond films has an impact on the electronic properties, efficiency, and sensitivity of diamond-based detectors [12]. The existence of defects in diamond films is accredited to the modification of the electrical properties. In the case of a low boron concentration, single substitution defects are more predominant, while more complex defects like B dimers have appeared with the enhancement of the boron concentration [13].At a very high-boron concentration, impurity states are combined and result in metal-like conductivity [14]. The very high doping of boron in diamond mainly leads to hopping conductivity [15].

Diamond could be integrated with other allotropic forms of carbon and polymers for various robust applications [16–19]. The pick-up and drop method is a simple technique for transferring nanocrystalline diamond films from the growth substrates to two-dimensional crystals for the fabrication of heterostructure devices [18]. Bogdanowicz et al. reported the synthesis of free-standing boron-doped diamond nanosheets (BDDNSs) and the transferring of those diamond nanosheets onto graphene to fabricate BDDNS heterostructures, and also investigated the characteristics of a low-temperature diamond-based transistor using BDDNSs [19]. A boron-doped diamond (BDD) electrode was modified by Nafion polymer and the Nafion-BDD electrode utilized as a sensor to detect caffeine, with this sensor exhibiting high sensitivity and reproducibility, while being faster and more reliable in comparison to electrodes like glassy carbon [20]. Moreover, enhanced heat transfer rates and reduced thermal expansion coefficients have been observed for a 3D-printed diamond-polymer composite material, which has excellent potential as heat sinks and cooling coils for electronic devices [21]. Babchenko et al. developed a diamond-polydimethylsiloxane (PDMS) transparent-microfluidic system with high conductivity (dimension of the electrically active layer varied between 100 and 500 μm), and optical transparency for electrical and optical monitoring of cells [22]. BDD thin films exhibited outstanding mechanical properties like high hardness and toughness, and robust thermal stability, to be utilized as wear-resistant thermal coatings in high-temperature oxidizing atmospheres [23]. High boron-doped diamond films demonstrated elastic-mechanical softening and slightly reduced elastic and mechanical properties compared to the pure diamond [24]. Diamond is known as a material with high hardness and durability, but its brittle nature results in quick deformation, therefore, investigation of the electro-mechanical properties of BDD electrodes has enormous scope in various applications like strain and piezoelectric sensors [25]. Fabrication of free-standing high-boron doped diamond on polymer platforms shows the pathway for flexible BDD-based sensors to be utilized in strain and piezoelectric kinds of sensor applications.

In the present study, we demonstrated the fabrication of boron-doped diamond nanosheets (BDDNS) on polymer substrates. The size of flexible BDD electrodes utilized in sensing applications is in the order of microns [26], here we reported a free-standing and flexible BDD nanosheet with a size of 1 cm X 1 cm. The influence of mechanical strain on the electrical properties of high doped BDDNS has not been investigated yet. Before studying the electro-mechanical properties, the detailed surface morphology and bonding characteristics were analyzed for the top and bottom surfaces of the BDDNSs. A Kelvin probe force microscope was used to examine the contact potential difference and calculate the work function of the BDDNS's bottom and top surfaces. Before measuring the electro-mechanical properties, resistance mapping and Hall measurements were performed to observe the conducting capability and then investigate the change in electrical resistance of the BDDNS/Kapton as a function of mechanical strain applied by bending of the BDDNS/Kapton device.

## 2. Experimental Methods

### 2.1 BDD thin film growth

The BDDNSs were synthesized in a microwave plasma-assisted chemical vapor deposition (MW-PACVD, 2.45 GHz) system (Seki Technotron AX5400S, Japan). The boron doping into diamond films was performed using diborane ($B_2H_6$) as a dopant precursor, and the [B]/[C] ratio was maintained at 10000 ppm. The tantalum substrates (Sigma-Aldrich Chemie, with a thickness of 0.025 mm, and 99.9+% metal basis) were placed in the chamber, and a microwave power of 1100 W applied during the growth process. The substrates were heated up to 500 $^0$C during the growth of the BDD films. The BDD thin films were grown for time of 300 min, resulting in a ~1.5 μm thickness. Before the BDD growth process, all of the tantalum (Ta) substrates were cleaned using the RCA method. The nucleation process on these substrates was performed using a slurry consisting of undoped nanodiamonds with sizes ~4–7 nm. The nanodiamond seeding density was approximately ~2 x $10^{11}$ $cm^{-2}$ for Ta substrates [27]. In order to demonstrate the morphology of seeded Ta substrates, scanning electron microscopy (SEM) images were collected from the bare Ta, and ND seeded Ta substrates (see Figure S1).

## 2.2 BDDNS-Kapton structure preparation

The schematic diagram of the fabrication process of the diamond (top surface)/Kapton structure is presented in Fig. 1a. In the first step, a PDMS-based gel (Gel-Pak, USA) was deposited on the BDD/Ta substrate. In the next step, the BDD-PDMS was mechanically removed from the tantalum substrate and transferred to the Kapton tape with a thickness of 0.025 mm (3M, Europe). Then, the

PDMS was mechanically removed. To prepare the diamond (bottom side)/Kapton structure, we replaced the PDMS with the Kapton, as shown in Fig. 1b. To perform the studies on the BDDNSs, we used both the top and bottom surfaces of the BDDNSs (dimension of BDDNSs ~1cm x 1 cm).

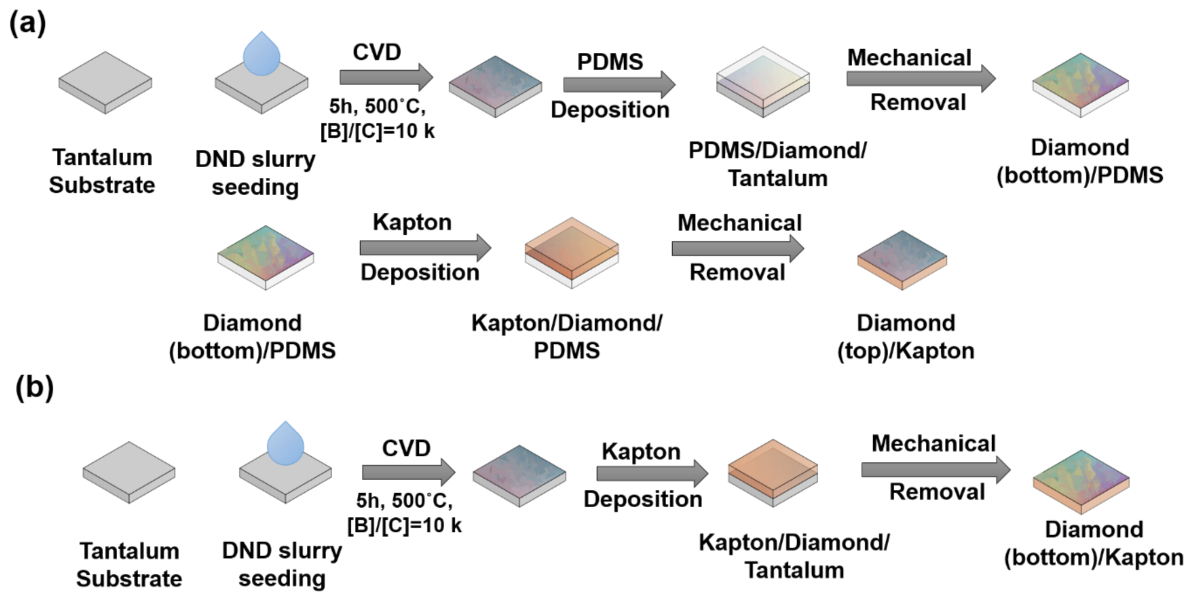

**Fig. 1.** Growth and fabrication of BDDNSs: (a) Top-surface/Kapton, and (b) Back-surface/Kapton structur

## 2.3 Morphology and AFM topography

The surface morphology of the BDDNSs was studied using high-resolution SEM (FEI Quanta FEG 250) with a 10 kV beam accelerating voltage, a secondary electron-Everhart-Thornley detector, and high vacuum mode (pressure $10^{-4}$ Pa). The surface topography was examined by atomic force microscopy (AFM), and Kelvin probe force microscopy (KPFM). Measurements were performed using a Veeco/Bruker Nanoman V microscope equipped with a Nanoscope V controller. Before the KPFM measurements, the BDDNSs were attached to the substrate using electrically conductive silver paint (Silver Conductive Adhesive 503, Electron Microscopy Sciences), and the BDDNS samples were grounded to measure the contact potential difference (CPD). The CPD results were observed using the lift mode, also called the two-pass technique. In this mode, each line must be scanned twice, the first scan represents the topography of the surface in tapping mode, and the second one is considered at a certain distance (lift-up height) relative to the surface where surface charge or the contact potential difference is measured. In the present study, the typical lift-up height of ~50–150 nm was maintained to avoid the unintentional contact of the scanning tip on the sample. Bruker PFQNE-Al probes with a typical spring constant of 0.8 N/m and resonant frequency of 300 kHz, and silicon tips with a tip radius of 5 nm on a silicon nitride cantilever were used for scanning. The CPD of the sample was estimated based on the CPD histogram taken from the whole scanned area. The work function of the samples was calculated based on the calibration using a material with a known work function. In the present study, highly oriented pyrolytic graphite (HOPG, WF ~4.6 eV) was used for calibration. The percentage of grain size distribution was estimated as follows, first, every grain was manually outlined in a certain area, then grain size was calculated using Gwyddion software.

Based on the obtained results, four different grain sizes distributions have been denoted and their probability of appearance on the top/bottom side is listed in Table 1.

### 2.4 Raman spectra and mapping

The Raman Spectroscopy measurements of the BDDNSs were performed using a Horiba Jobin Yvon T64000 spectrometer equipped with a single grating and an automated 3-axis stage with 100 nm spatial resolution. The excitation source was a Kimmon Koha He-Cd dual-mode (325 nm/422 nm) laser. The 422 nm wavelength laser light and satellite lines were removed with a series of optical filters. The laser light with a power of 23 mW was focused on the BDDNS sample using an Olympus MPFLN objective with 50x magnification. This setup allowed for the acquisition of wide-range spectra in both single points and also maps with a sub-micron lateral scale. The analysis of the Raman spectra was conducted in the Wolfram Mathematica 11.2.0.0 software.

### 2.5 Electrical properties

The resistance of the BDDNSs was measured on both sides at room temperature by a two-point probe. The needles with a diameter of 20 μm were connected to the measuring source unit (Keithley 2400, UK) via two micro-positioners (Signature S-725, USA), which were mounted on the x-y stage. The resistivity contour mapping of the BDDNSs was recorded using a microscope (Delta SZ-630, Poland) and CMOS camera (DLT-Cam pro 20MP, Poland). The voltage drop across the probes was measured as a function of the current (1 mA). Hall effect measurements were performed in the Van der Pauw configuration (0.55 T Ecopia HMS-3000) to observe the conductivity and polarity of the high doped BDDNSs.

### 2.6 Electro-mechanical properties

To analyze the electro-mechanical properties of the BDDNS/Kapton device, we constructed an apparatus, and the custom-built system was used to measure the resistance as a function of the applied strain. Fig. 2a and b shows a schematic representation of before and after the BDDNS/Kapton device's mechanical-bending. The strain was introduced by a micrometer screw moved from 0 % to 1.5 %. The BDDNS sample (1 cm x 1 cm x 1.3 μm) on Kapton tape (1.2 cm x 1.1 cm x 25 μm) was connected to the measurement unit (Keithley 2400, UK) via platinum wires with diameters of 30 μm [Fig. 2a and b]. Before the measurement, the contacts were fixed using silver paste (EPO-TEK H20E, Epoxy Technology, USA), and the fixed sample was heated at 70°C for 18h in a vacuum oven (DZ-2BC II, Chemland, Poland). The bending radius (BDD/Kapton) was estimated from the individual images of each bending. To capture the image, we used a CMOS camera (DCC1240C, Thorlabs, USA) with a 1.8/125 mm lens (Meopta Largor, Czech Republic). Image processing was performed using a custom made program written in Python 2.7.2 software on a standard PC. The extrapolated bend radius and the distance from the neutral axis were used to determine the strain. All measurements were conducted at room temperature (22 °C, 44 % RH) in a cleanroom. The microscope images were captured with a microscope (LAB 40 POL, OPTA-TECH, Poland). Fig. 2c and d show the photographs of the BDDNS/Kapton device before and after mechanical-bending.

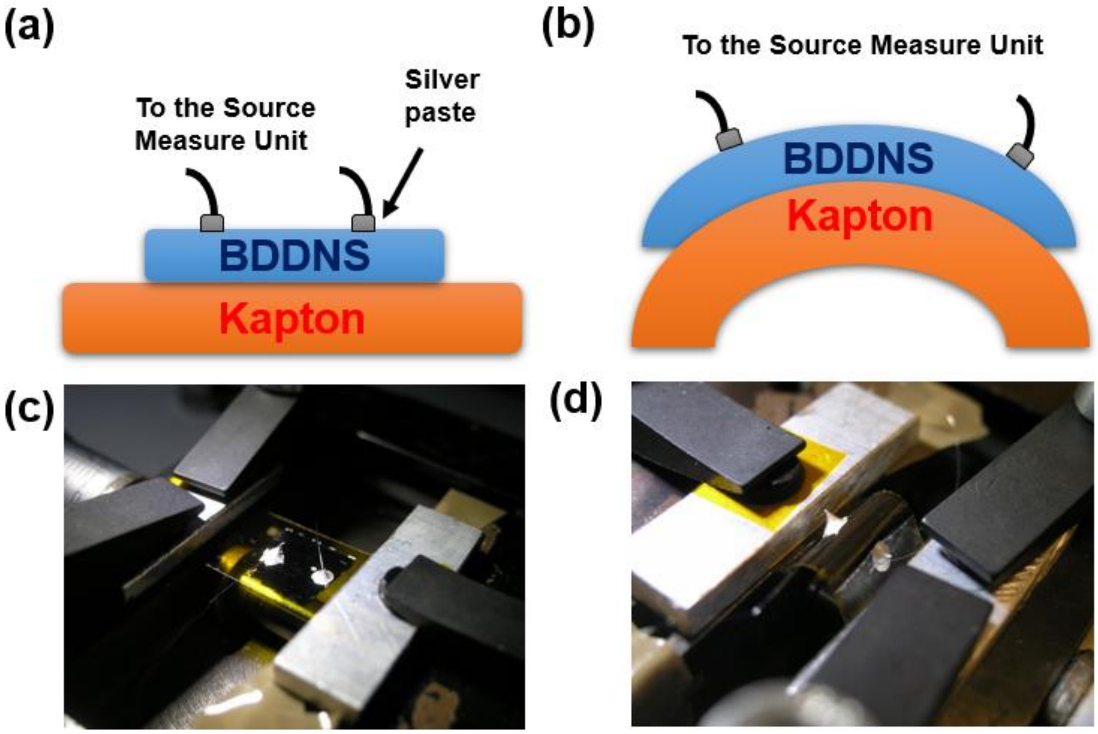

**Fig. 2.** Mechanical bending experimental setup: (a) schematic diagram of before bending, (b) after bending, photographs of BDDNS/Kapton (c) before bending, (d) bending position

## 3. Results and Discussion

### 3.1. Morphological studies of diamond nanosheets

Fig. 3a shows the surface morphology of the BDDNS's topside view after three hours of growth, which demonstrates the faceted diamond grains of various sizes due to the high boron doping. The high-boron doping level of diamond growth results in an increase of nucleation after the first step of growth and consequently reduced diamond grain size, low growth rate, and low roughness [28,29]. The BDD grains are non-spherical and oriented in various directions due to random nucleation [30]. The number of {111} faceted grains increased by the addition of the boron dopant in diamond growth plasma, and however most defects also contain {111} faceted grains [31]. The surface morphology of the bottom side of the BDDNS is shown in Fig. 3b. The bottom surface of the BDDNS appears to be smoother, consisting of smaller, spherical, fine grains. The different morphology of the BDDNS bottom side is due to the initial growth of the BDD films starting from the spherical nucleation sites, and the intrinsic nature of the columnar structure can be perceived after certain growth times. Even high-level boron doping also induces the second nucleation after the first step of growth, as mentioned earlier, which also results in smaller and spherical grains on the bottom side. Cross-sectional SEM, collected to measure the film thickness and to observe the columnar structure [Fig. 3c], depicts a columnar growth structure of BDD with a thickness of 1.5 μm. Additionally, for detailed information on the diamond grain size distribution in the BDD sheets, four different areas of grains were taken into consideration and their % of occupancy on the top and bottom sides of the BDDNSs (Table. 1).

Table 1. Grain size occupancy over boron-doped diamond film

| Grain size | Top side | Bottom side |
|---|---|---|
| < 160 nm | 12.5 % | 18 % |
| 160 – 220 nm | 29 % | 59 % |
| 220 – 280 nm | 33 % | 18 % |
| > 280 nm | 25.5 % | 5 % |

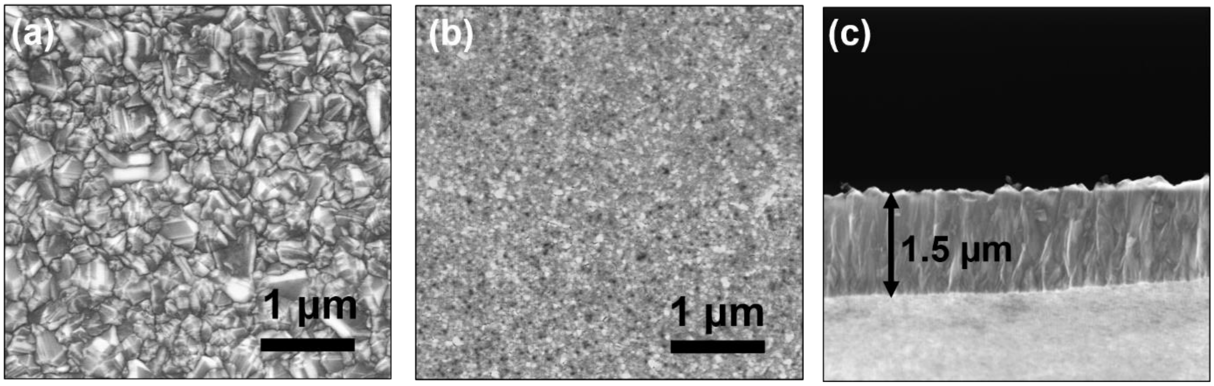

**Fig**. **3.** SEM image of BDDNSs, (a) top surface, (b) bottom surface, and (c) cross-sectional view

AFM topography over a 10 μm x 10 μm area allowed us to investigate the roughness and grain morphology of the top and bottom sides of the BDDNSs. The AFM topography of the BDDNS's top and bottom surfaces are shown in Fig. 4a and c, respectively. The top surface of the BDDNS reveals a high amount of BDD crystallites in random growth directions with a root mean square roughness (Rq) value of 67 nm and average roughness (Ra) of 54 nm. Whereas the bottom surface depicts a flat, surface without any faceted grains, with the Rq and Ra values decreased up to 12 nm and 10 nm, respectively. The grain morphology of the BDDNS's top surface illustrates the high roughness due to the sharp edges of faceted grains. High boron doping induces the formation of small grains and the dispersion of small grains in the matrix of large faceted grains, as results of secondary nucleation induced by the presence of boron in the diamond growth plasma [28–30]. AFM topography of the bottom surface of the BDDNSs reveals a smoother surface due to the small and fine grain distribution.

Fig. 4b and d show the CPD images of the BDDNS's top and bottom surfaces. It should be noted that these measurements were carried out at room temperature and ambient atmospheric conditions.

The CPD image of BDDNS's top surface demonstrate CPD values between – 0.67 V to – 0.78 V, whereas the bottom surface reveals CPD values between – 0.70 V to – 0.78 V. Work function values of 4.69±0.02 eV and 4.70±0.01 eV for the BDDNSs are achieved for the top and bottom surface respectively. These results indicate that the CPD values do not vary significantly with the morphology and size of the BDD grains. Next, the BDD nanosheets have been removed mechanically from the Ta substrate. This process might result in partial detachment of degenerated Ta-diamond interface including insulating seeds This fact jointly with encapsulating overgrowth of seeds by BDD could be attributed as a reason for similar CPD values for both sides of BDDNSs in our work. Nevertheless, this effect is unclear and requires farther nanoscopic investigations.

The observed CPD slope could be attributed to the sample inclination or minor potential differences between the electrode grounding and a scanning probe. Those effects were not filtered to present the original, physical CPD data. We will expect, their influence on the average value of CPD can be minor, as they rather broaden CPD's standard deviation. Taking into account obtained results, we predict electrostatic charge originating from tip or substrate could be negligible in our case. As in Fig. 4b we don't expect visible effect of induced charging, though, Fig. 4d possibly illustrates small areas where the physical contact between sample and tip could induce charging of the sample surface. The maximum CPD dip resultant from this charging is approximately 30 – 40 mV. Obtained values are much smaller than those observed by Verveniotis et al. [32]. This observation could be an effect of relatively fast discharging of the surface due to the conductive nature of BDDNS's. Phase images of both BDDNS's top and bottom surfaces demonstrated a uniform material composition (data not shown here).

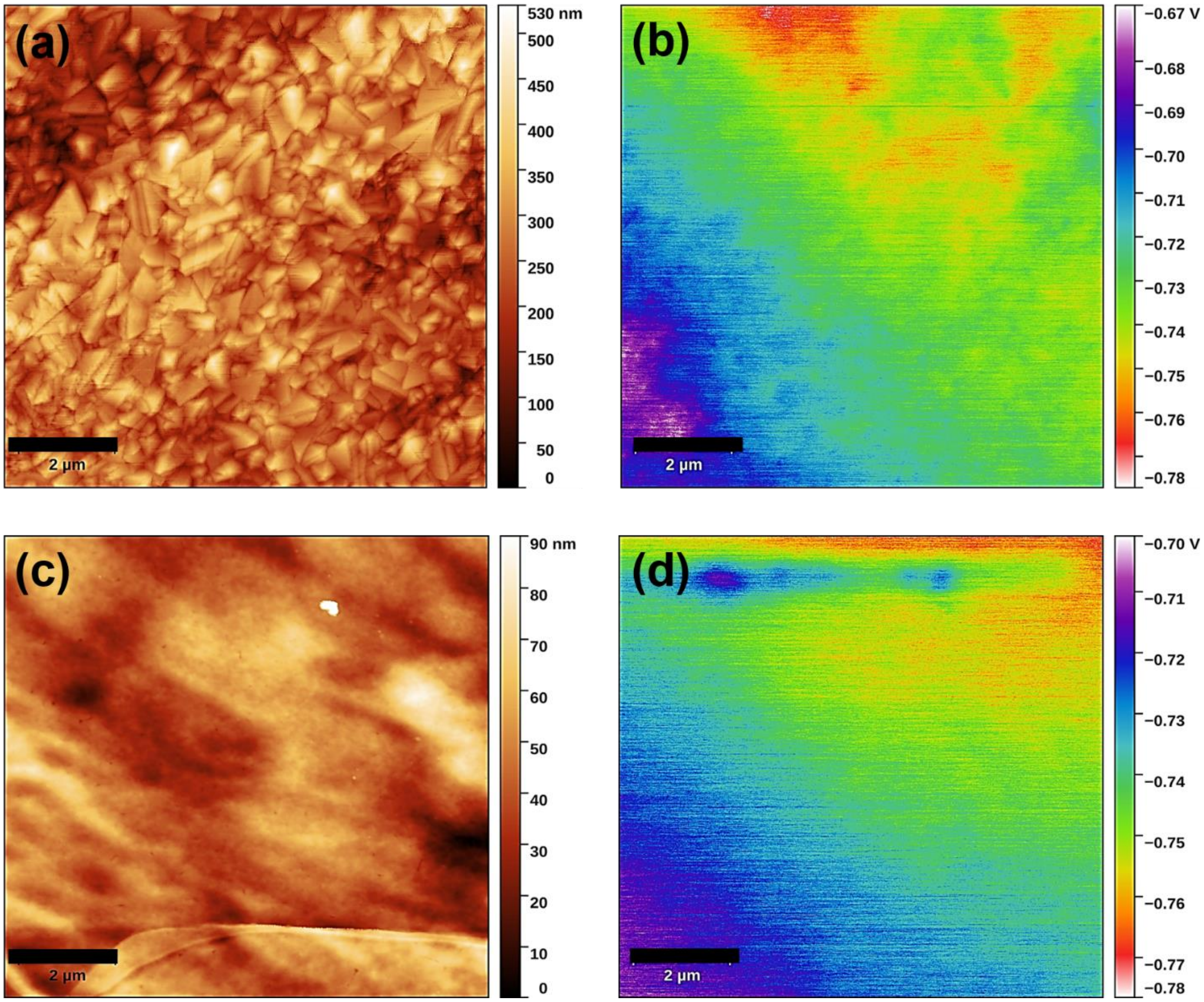

**Fig. 4.** AFM topography images of high-boron doped (a) BDDNS top surface, and (c) BDDNS bottom surface. AFM contact potential difference distribution images of (b) BDDNS top surface, (d) BDDNS bottom surface. [scale bar ~2 µm]

### 3.2. Raman spectroscopy and mapping of BDDNSs

The Raman spectroscopy measurements were carried out on BDDNSs, and to collect the Raman spectra of the top and bottom surfaces, $SiO_2/Si$ substrates were used to place the BDDNSs. Fig. 5a and d depict three lines within the range of 1300 –1600 $cm^{-1}$, which are associated with different phases of carbon. The sharp peak of the BDDNSs located at around 1331 $cm^{-1}$ is attributed to the $sp^3$ hybridization of carbon [31]. This peak is narrow and intensive, indicating the successful growth of the diamond layer and the high quality of that material. The other two Raman features located at 1570 $cm^{-1}$ (G-band) and 1390 $cm^{-1}$ (D-band) emerged from the $sp^2$ hybridization of carbon [33]. Therefore, the presence of G- and D-bands are clear evidence of non-diamond materials in the BDDNSs [7]. Furthermore, two more lines were found in the Raman spectra of the BDDNSs. The line located at around 850 $cm^{-1}$ is attributed to bonds between silicon and oxygen atoms [34], which raised from the substrate. The featured line illustrated at a Raman shift of about 500 $cm^{-1}$ was observed only for the top surface of the BDDNSs [Fig. 5a]. This line is related to vibrations of the boron structures [35,36], and it is clear evidence of a significant level of boron doping.

The above-described spectral lines were analyzed during mapping measurements of the samples. Each of the lines was fitted with Lorentz curve fitting to estimate the parameters of the line, such as, position, intensity (in terms of integration of the curve), and full width at half maximum (FWHM). These measurements revealed that the samples were fairly uniform in their structure. The $sp^3$ peak position in the Raman spectra on the top surface of the BDDNSs [Fig.5b], was equal to $1331.04 \pm 0.10$ $cm^{-1}$. This value is slightly lower than that of the bottom surface of the BDDNSs [37], indicating minor tensile strain in the structure. This tensile strain might be originating from the higher level of boron doping, while the bottom surface of the BDDNSs reveals the $sp^3$ peak at ~ 1331.80 ± 0.16 $cm^{-1}$ [Fig. 5e]. In both instances, the shift in the Raman peak position from natural diamond is quite low, indicating the uniformity and high quality of the material.

The density of the graphitic inclusions is slightly more inhomogeneous throughout the surface, indicating a degree of variation of the nanodiamond grain sizes, as seen by the non-uniformity of the $sp^3/sp^2$ ratio maps [Fig. 5c and Fig. 5f]. The average ratio of intensities between $sp^3$ and $sp^2$ lines is 0.66 ± 0.08 in the case of the top surface of the BDDNSs [Fig. 5c], while the value is 0.74 ± 0.07 for the bottom surface of the BDDNSs [Fig. 5f]. Nonetheless, to correlate with the strain of the materials, this difference is very slight. However, it can be attributed to the difference in the doping of the material. In such a case, it might be that the rate of boron incorporation is prominent at the grain boundaries. It is worth noting that, while the peak intensity ratio seems low, similar $sp^2$ and $sp^3$ ratios are shown in materials grown by other groups [7,31].

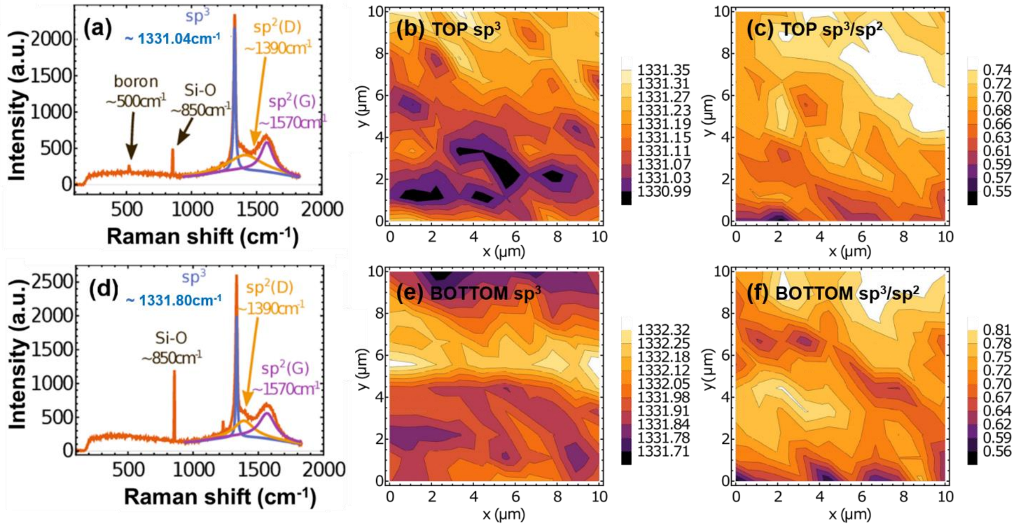

**Fig. 5.** Raman spectroscopy of (a) BDDNS top surface, (d) BDDNS bottom surface. Raman mapping of BDDNS top surface, (b) $sp^3$ mapping, (c) $sp^3/sp^2$ mapping. Raman mapping of BDDNS bottom surface, (e) $sp^3$ mapping, (f) $sp^3/sp^2$ mapping.

### 3.3. Electrical resistance mapping of BDDNSs

The electrical resistance mapping of the BDDNSs was carried out using a two-point probe technique for both sides of the BDDNS/Kapton, and the mapping performed over an area of 3.5 x 3.5 mm. The obtained results are shown in Fig. 6. Fig. 6a reveals the resistance mapping of the top surface of the BDDNS with an average resistance value of 66 Ω. Whereas the bottom surface showed a resistance of 4.4 kΩ [Fig. 6b]. It should be noted that even for the BDDNS prepared with unique processing parameters throughout the growth process, a significant variation in resistance was observed between the top and bottom surfaces. The resistance of both surfaces is unevenly varied due to the non-uniform distribution of boron throughout the BDDNSs.

The high resistance characteristics of the bottom surface are due to boron suppression during the initial growth by the presence of oxygen [38]. The other reason for high resistance is defects/damage caused by the process of transferring the BDDNS to the Kapton, and uneven boron doping during the CVD process. Moreover, all of the doped boron atoms could not contribute to the conductivity of the BDD films because more than 10 % of the doped boron atoms do not act as acceptors; some of them may be passivated by connecting with other impurities like hydrogen, and some of them might be inactive [39,40]. In the case of polycrystalline BDD films, the boron tends to segregate at grain boundaries and retain as inert impurity [31]. Therefore, the initially incorporated boron atoms were probably placed at grain boundaries. Therefore, even the bottom surface being smoother, consisting of small, fine grains, exhibited high resistance compared to the top surface. Furthermore, it has been suggested that conductivity in BDD comes mostly from the holes, not from the electrons [8], therefore the smaller grains and the high number of grain boundaries does not lead to high conductivity. The low resistance characteristics of the top surface are due to the large BDD grains, as the hole mobility of the BDD films was enhanced for large BDD grains [31,41].

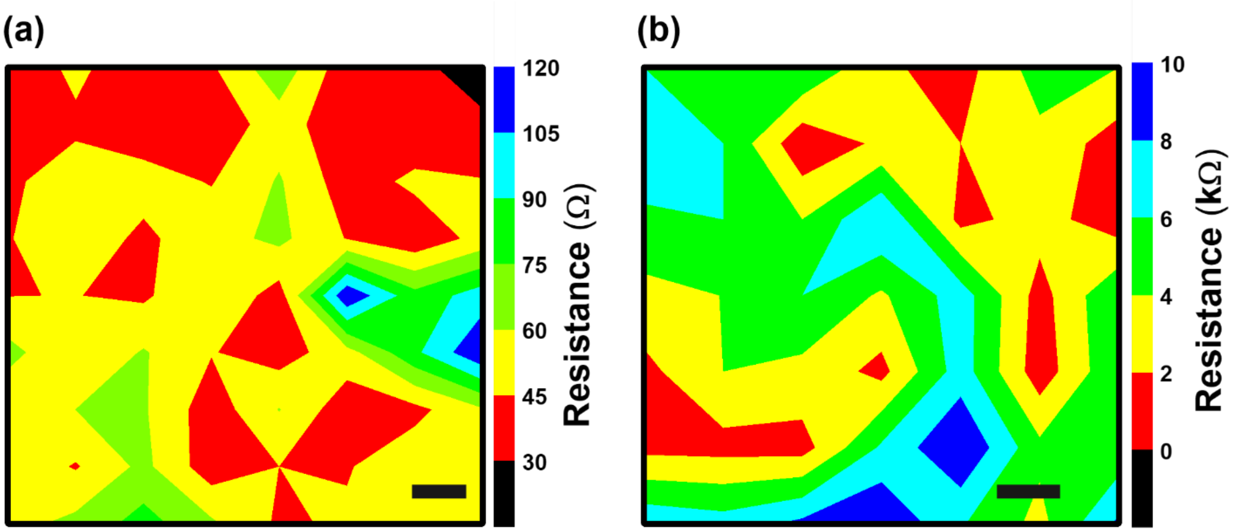

**Fig. 6.** Resistance mapping of high-boron doped, (a) BDDNS's top surface, and (b) BDDNS's bottom surface (Scale bar ~ 500 µm)

In order to measure the charge carrier density and mobility, Hall measurements were carried out using the Van der Pauw method, and the obtained results are presented in Table 2. The polarity of the Hall voltage indicates that high-boron doped BDDNSs are demonstrating p-type conductivity. The charge carrier density and mobility values of the top surface of the BDDNSs reveal a value of 6.19 x $10^{19}$. $cm^{-3}$ and 9 $cm^2.V^{-1}. s^{-1}$, respectively. While the bottom surface showed the lower charge carrier density and high mobility vales compared to the BDDNS's top surface with a value of 1.11 x $10^{17}$ $cm^{-3}$ and 417.5 $cm^2.V^{-1}. s^{-1}$. The Hall results of the charge carrier density resulting from the top surface of the BDDNS reveal the agreement with resistance mapping results of the top surface. Also, they confirm that the high boron concentration in the large grains (top side) resulted in a high carrier concentration and decreases in the mean free time between the carriers [42]. However, the Hall mobility results divulge a disagreement with the resistance mapping results, as the top surface showed deficient mobility, while the bottom surface exhibited a high mobility value. The high mobility of the bottom surface is due to the presence of small diamond grains, which results in a high number of grain boundaries to act as conducting paths for the charge transfer process [19]. The present results divulged that the hole mobility of BDD could be augmented by small diamond grains, and this result is a contradiction to the previous report, which stated that hole mobility could be increased by grain size [41].

**Table 2. Electrical properties of the BDDNSs**

| **Sample** | **Charge carrier density ($cm^{-3}$)** | **Hall mobility ($cm^2$ $V^{-1}s^{-1}$)** | **Resistivity (Ω·cm)** |
|---|---|---|---|
| Top surface | $6.19 \cdot 10^{19}$ | 9 | 0.01 |
| Bottom surface | $1.11 \cdot 10^{17}$ | 417.5 | 0.13 |

### 3.2. Electro-Mechanical properties of BDDNSs

A custom-made system was designed to measure the electro-mechanical properties of BDDNS/Kapton, which was used to measure the voltage-current (V-I) characteristics as a function of applied strain. The BDDNS was placed upside down for the fabrication of the BDDNS/Kapton device to utilize the smooth surface for better contact for connecting wires of the source measure unit. The obtained result of the mean electrical resistance (measured using a two-point probe) of the BDDNS/Kapton structure vs. strain is presented in Fig. 7a. The measured BDDNS sample size was ~1 cm x 1 cm x 1.3 μm, placed on Kapton tape with a size of 1.2 cm x 1.1 cm x 25 μm. Fig. 7a depicts the non-linear response of the residual electrical resistance ($\Delta R / R_o$) change with applied strain. The $\Delta R / R_o$ of the BDDNS/Kapton varied in three different stages with an increment of the applied strain. In case of the “stage 1”, the $\Delta R / R_o$ increased step-wise with the applied strain. The inset in Fig. 7a shows an enlarged view of the “stage 1” result, which reveals a step-wise increase of the $\Delta R / R_o$ up to 9 % at an applied strain of 0.14 %.

Then, for an applied strain of 0.14 % to 0.47 %, the $\Delta R / R_o$ increased from 9 to 9.87 % [“stage 2”]. Further, in “stage 3”, the $\Delta R / R_o$ of the BDDNS/Kapton structure increased sharply from 9.87 % to 26.26 %, with a strain of 0.47 % to 0.55 %. It should be noted that a further increment of strain after 0.55 % leads to the formation of cracks in the BDDNS/Kapton device and results in damage to the device, which could be considered as a threshold value for use in practical applications. The variation in the $\Delta R / R_o$ of the BDDNS/Kapton device with applied strain might be due to variation in the residual stress of the BDDNS foil, defects, and/or the presence of non-diamond carbon at the grain boundaries. The stress in the BDDNS/Kapton is intrinsic tensile stress, which increases with the boron concentration [43]. In the present study, high doped BDDNS foils were utilized, and as a result, tensile stress existed in the BDDNS/Kapton device. The intrinsic tensile stress was estimated using the characteristic diamond peak positions of the BDDNS’s top and bottom surfaces [44]. The estimated residual tensile stress values are 1.04 GPa and 0.23 GPa for the top and bottom surfaces, respectively. Moreover, the induced tensile stress might be produced during the mechanical bending of the BDDNS/Kapton.

In order to exhibit the BDDNS/Kapton structure's appearance during the mechanical bending, a schematic representation is shown in Fig. 7b. The schematic presentation of the “stage 1” bending position of the BDDNS/Kapton depicts the elongation of the BDD grains, which causes the generation of tensile stress by the mechanical bending process. Besides this, boron precipitation occurs at the grain boundaries, and the existence of dislocations for the high boron-doped diamond results in the suppression of grain boundary relaxation [43]. Moreover, apart from the boron doping levels and inhomogeneous distribution, the residual stress in the BDDNSs ensued due to the high density of defects, dislocations at the grain boundaries, the crystal texture, and $sp^2$ carbon and grain size [45,46]. The tensile stress generated by the externally applied strain causes the increasing of the distance between the conducting grains and $sp^2$ clusters, resulting in the increasing the distance between conducting states. Therefore, the $\Delta R / R_o$ of the BDDNS/Kapton devices increase under tensile strain. In addition, a high piezoresistive effect was reported for hydrogen-terminated nanocrystalline diamond due to strain-induced changes in the resistivity of the grain boundaries [47]. However, the conductivity in BDD films is primarily from the holes, and the hole conductivity is dominant in large grains [41]. Nevertheless, the top side of the BDDNS/Kapton device was the bottom surface of the BDD foil, which consisted of small BDD grains. Therefore, the conductivity of the BDDNS's bottom-surface might be due to conducting channels formed by the $sp^2$ carbon clusters, the distance between these $sp^2$ carbon clusters increased while applying the tensile strain, and increased the $\Delta R / R_o$.

Further, the change in the $\Delta R / R_o$ with strain is relatively low, even negligible in "stage 2". Such a minor change of residual resistance because of the distance between the $sp^2$ grains might reach saturation and have no further influence from strain. The appearance of the BDDNS/Kapton at "stage 2" is shown schematically in Fig. 7b. A further increase of strain resulted in high tensile stress and led to the formation of cracks in the BDDNS/Kapton device, resulting in an abrupt increase of $\Delta R / R_o$. This is called the fracture point, and at this point, failure of the device was noticed. The appearance of the BDDNS/Kapton device at "stage 3" is shown schematically in Fig. 7b. To investigate the stress in strained BDDNS/Kapton samples, Raman spectroscopy measurements were performed on strained, and unstrained BDDNS/Kapton samples (Figure S2). The stress values were calculated using the peak shift of diamond Raman line [44]. The achieved Raman results revealed that the stress in strained BDDNS/Kapton

(~5.94GPa) increased significantly, compared to the stress in the unstrained BDDNS/Kapton sample (~3.78 GPa).

Finally, the proposed BDDNS/Kapton device showed the capability to perform as a strain sensor or piezoresistive sensor at applied strain ranges between 0 and 0.55 %, which showed the pathway for the development of a low-strain sensor. Furthermore, we have presented the comparison of our results with CNTs, Graphene, and metal-based strain sensors in the Table. 3. The gauge factors (GF) at different applied strain has been calculated and shown. The BDDNS/Kapton strain sensor exhibited the GF values from 16.26 to 66.74. However, the GF value is primarily depending on the conductivity of materials, higher the conductivity tends to low GFs. Furthermore, the sensitivity of BDDNS/Kapton strain sensor has been shown the sensitivity of 0.55 %.

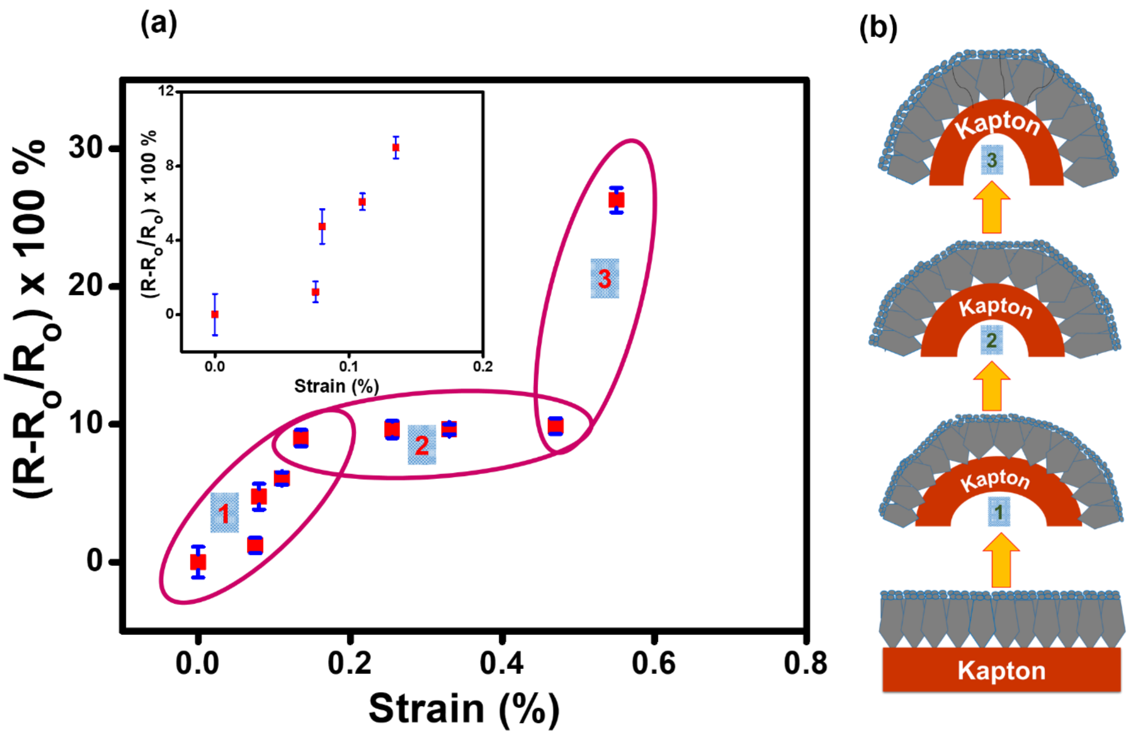

**Fig. 7.** Electro-mechanical bending results of high-boron doped BDDNS/Kapton, (a) Normalized change in resistance while applying strain to the BDDNS/Kapton structure [Inset shows the enlarged view at strain ranges between 0 and 0.14 %]. (b) Schematic presentation of BDDNS/Kapton, before and during the bending by employing the strain.

**Table. 3.** Comparison of strain sensors fabricated with different materials

*GF = $\frac{\frac{\Delta R}{R}}{\varepsilon}$ , $\frac{\Delta R}{R}$ = Residual electrical resistance, ε = Strain

| **Strain sensors** | Material | Strain range (%) | Linearity | Gauge Factor (GF)* |
|---|---|---|---|---|
| Ref. [48] | Ag/PDMS | 36 | Linear | 939 |
| Ref. [49] | PDMS/AgNW/PDMS | 70 | Partly linear | 2-14 |
| Ref. [50] | MWCNTs/PDMS | 45 | Nonlinear | 1.2 |
| Ref. [51] | CNT/PDMS | 100 | Nonlinear | 2 x $10^4$ |
| Ref. [52] | Graphene | 1.5 | Linear | 150 |
| Ref. [53] | Graphene/PDMS | 7.1 | Two linear regions | 2.4-14 |

| | | | | |
|---|---|---|---|---|
| Ref. [54] | Graphene/PDMS | 1.6 | Linear | 546 |
| Present work | BDDNS/Kapton | 0.55 | Nonlinear | 16.26–66.74 |

In order to investigate the performance of our BDDNS/Kapton strain sensor, different strain values were applied for a constant time period of 5 min. Fig. 8 shows the performance of the BDDNS/Kapton strain sensor at applied strain values of 0.09, 0.11, and 0.15. The strain was applied by bending the sensor, as a result, the applied strain on the device has been increased from 0 to 0.09, while the resistance has been increased to a certain value. The constant strain of 0.09 was applied for 5 min, then the applied strain was reduced to 0. However, device resistance has been not reached to initial resistance value. Next step, the applied strain has been increased to value of 0.11 and applied time was 5 min, and then applied strain decreased to ‘0’. Like the first case, the initial resistance again increased even after removing the strain. For the third time, the strain has been increased from 0 to 0.15 by bending the BDDNS/Kapton sensor, and the device kept under the strain of 0.15 for 5 min. Then strain has been removed by releasing the bending of the BDDNS/Kapton device. The resistance variation trend of the bending sensor under a series of increasing strain from 0.09 to 0.15 is in good agreement with results obtained by Cheng et al. [55] for the graphene-based fiber sensor , therefore, the represented results of BDDNS/Kapton strain sensor has been shown that its operation is stable and reproducible. The increase in initial resistance even after the removal of applied strain might be due to an increase in intrinsic tensile strain by bending of the BDDNS/Kapton device. Therefore, even after removing the applied strain, the presence of intrinsic strain causes a slight increase in initial resistance. A similar phenomenon was observed for extremely stretchable strain sensors based on cross-links hydrogels [56], and carbon nanotubes/isoprene rubber (IR) composites [57].

Therefore, the proposed BDDNS/Kapton strain sensor shown good repeatability and stability to employ in practical applications.

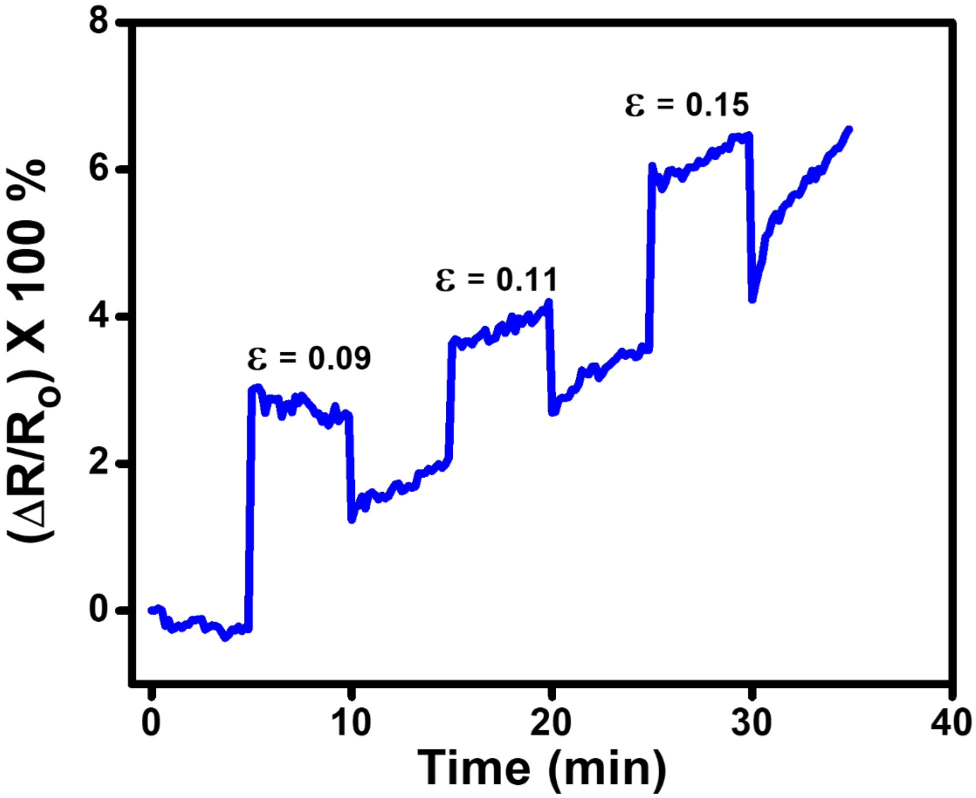

**Fig. 8.** BDDNS/Kapton strain sensor performance at different applied strain value of 0.09, 0.11 and 0.15.

In the present study, the electromechanical properties of BDDNSs were investigated for BDDNSs fabricated with unique conditions. But the role of morphology and microstructure on flexibility and electromechanical properties of BDDNS/Kapton has been not completely demonstrated. We intend to continue on this work by varying the growth conditions to obtain different morphological and microstructural BDDNSs to fabricate BDDNS/Kapton sensors and investigating the electromechanical performance.

## 4. Conclusion

High conducting BDDNS were fabricated and transferred to a flexible polymer Kapton substrate. Different surface morphologies were observed for the top and bottom sides of the BDDNS foils, the top side showing large, faceted grains while the bottom side showed a smooth surface with small, fine grains. A surface roughness Rq of 67 nm was observed for the top surface, whereas a low surface roughness Rq of 12 nm was attained for the bottom surface. A Kelvin probe AFM measured the work function results and revealed values of 4.69 eV and 4.70eV for the top and bottom surfaces of the BDDNS foils, respectively. Moreover, the top surface showed the average electrical resistance of 31 Ω, but the bottom surface showed high electrical resistance up to 10 kΩ. The electro-mechanical measurements of the BDDNS/Kapton device demonstrated the positive change in the $\Delta R/R_o$ with strain for employment as a strain sensor. The performance of BDDNS/Kapton strain sensor has been tested at different applied strains such as 0.09, 0.11 and 0.15 for time period of 5 min. Therefore, the proposed BDDNS/Kapton device has excellent potential in low-strain sensor applications.

**Acknowledgements:** *The authors gratefully acknowledge financial support from the National Science Centre (NCN) under Grant No. 2016/22/E/ST7/00102. The DS funds of the Faculty of Electronics, Telecommunications and Informatics of the Gdańsk University of Technology are also acknowledged.*

## Supplementary data

Supplementary data to this article can be found online at

## References:

[1] R.L. McCreery, Advanced Carbon Electrode Materials for Molecular Electrochemistry, Chem. Rev. 108 (2008) 2646–2687. https://doi.org/10.1021/cr068076m.

[2] J. Asmussen, D. Reinhard, D. Reinhard, Diamond Films Handbook, CRC Press, 2002. https://doi.org/10.1201/9780203910603.

[3] Y. Wu, F. Jelezko, M.B. Plenio, T. Weil, Diamond Quantum Devices in Biology, Angewandte Chemie International Edition. 55 (2016) 6586–6598. https://doi.org/10.1002/anie.201506556.

[4] J.Y. Tsao, S. Chowdhury, M.A. Hollis, D. Jena, N.M. Johnson, K.A. Jones, R.J. Kaplar, S. Rajan, C.G.V. de Walle, E. Bellotti, C.L. Chua, R. Collazo, M.E. Coltrin, J.A. Cooper, K.R. Evans, S. Graham, T.A. Grotjohn, E.R. Heller, M. Higashiwaki, M.S. Islam, P.W. Juodawlkis, M.A. Khan, A.D. Koehler, J.H. Leach, U.K. Mishra, R.J. Nemanich, R.C.N. Pilawa- Podgurski, J.B. Shealy, Z. Sitar, M.J. Tadjer, A.F. Witulski, M. Wraback, J.A. Simmons, Ultrawide-Bandgap Semiconductors: Research Opportunities and Challenges, Advanced Electronic Materials. 4 (2018) 1600501. https://doi.org/10.1002/aelm.201600501.

[5] J.V. Macpherson, A practical guide to using boron doped diamond in electrochemical research, Phys. Chem. Chem. Phys. 17 (2015) 2935–2949. https://doi.org/10.1039/C4CP04022H.

[6] A. Kraft, Doped Diamond: A Compact Review on a New, Versatile Electrode Material, I.Nt. J. Electrochem. Sci. 2 (2007) 31.

[7] P.W. May, W.J. Ludlow, M. Hannaway, P.J. Heard, J.A. Smith, K.N. Rosser, Raman and conductivity studies of boron-doped microcrystalline diamond, facetted nanocrystalline diamond and cauliflower diamond films, Diamond and Related Materials. 17 (2008) 105–117. https://doi.org/10.1016/j.diamond.2007.11.005.

[8] W. Gajewski, P. Achatz, O.A. Williams, K. Haenen, E. Bustarret, M. Stutzmann, J.A. Garrido, Electronic and optical properties of boron-doped nanocrystalline diamond films, Phys. Rev. B. 79 (2009) 045206. https://doi.org/10.1103/PhysRevB.79.045206.

[9] V. Zuerbig, W. Pletschen, J. Hees, R.E. Sah, L. Kirste, N. Heidrich, C.E. Nebel, O. Ambacher, V. Lebedev, Transparent diamond electrodes for tunable micro-optical devices, Diamond and Related Materials. 38 (2013) 101–103. https://doi.org/10.1016/j.diamond.2013.06.010.

[10] T. Kondo, I. Neitzel, V.N. Mochalin, J. Urai, M. Yuasa, Y. Gogotsi, Electrical conductivity of thermally hydrogenated nanodiamond powders, Journal of Applied Physics. 113 (2013) 214307. https://doi.org/10.1063/1.4809549.

[11] T. Ikeda, K. Teii, C. Casiraghi, J. Robertson, A.C. Ferrari, Effect of the sp2 carbon phase on n-type conduction in nanodiamond films, Journal of Applied Physics. 104 (2008) 073720. https://doi.org/10.1063/1.2990061.

[12] Y. Ma, J. Tong, M. Zhuang, J. Liu, S. Cheng, X. Pei, H. Li, D. Sang, Superhydrophilic surface of oxidized freestanding CVD diamond films: Preparation and application to test solution conductivity, Results in Physics. 15 (2019) 102628. https://doi.org/10.1016/j.rinp.2019.102628.

[13] P. Ashcheulov, J. Šebera, A. Kovalenko, V. Petrák, F. Fendrych, M. Nesládek, A. Taylor, Z. Vlčková Živcová, O. Frank, L. Kavan, M. Dračínský, P. Hubík, J. Vacík, I. Kraus, I. Kratochvílová, Conductivity of boron-doped polycrystalline diamond films: influence of specific boron defects, Eur. Phys. J. B. 86 (2013) 443. https://doi.org/10.1140/epjb/e2013-40528-x.

[14] M. Ullah, E. Ahmed, F. Hussain, A.M. Rana, R. Raza, Electrical conductivity enhancement by boron-doping in diamond using first principle calculations, Applied Surface Science. 334 (2015) 40–44. https://doi.org/10.1016/j.apsusc.2014.07.157.

[15] R.F. Mamin, T. Inushima, Conductivity in boron-doped diamond, Phys. Rev. B. 63 (2001) 033201. https://doi.org/10.1103/PhysRevB.63.033201.

[16] P.-B. Li, Z.-L. Xiang, P. Rabl, F. Nori, Hybrid Quantum Device with Nitrogen-Vacancy Centers in Diamond Coupled to Carbon Nanotubes, Phys. Rev. Lett. 117 (2016) 015502. https://doi.org/10.1103/PhysRevLett.117.015502.

[17] B. Fan, Y. Zhu, R. Rechenberg, C.A. Rusinek, M.F. Becker, W. Li, Large-scale, all polycrystalline diamond structures transferred onto flexible Parylene-C films for neurotransmitter sensing, Lab Chip. 17 (2017) 3159–3167. https://doi.org/10.1039/C7LC00229G.

[18] V. Seshan, J.O. Island, R. van Leeuwen, W.J. Venstra, B.H. Schneider, S.D. Janssens, K. Haenen, E.J.R. Sudhölter, L.C.P.M. de Smet, H.S.J. van der Zant, G.A. Steele, A. Castellanos-Gomez, Pick-up and drop transfer of diamond nanosheets, Nanotechnology. 26 (2015) 125706. https://doi.org/10.1088/0957-4484/26/12/125706.

[19] R. Bogdanowicz, M. Ficek, M. Sobaszek, A. Nosek, Ł. Gołuński, J. Karczewski, A. Jaramillo- Botero, W.A. Goddard, M. Bockrath, T. Ossowski, Growth and Isolation of Large Area Boron-Doped Nanocrystalline Diamond Sheets: A Route toward Diamond-on-Graphene Heterojunction, Advanced Functional Materials. 29 (2019) 1805242. https://doi.org/10.1002/adfm.201805242.

[20] C.A. Martínez-Huitle, N. Suely Fernandes, S. Ferro, A. De Battisti, M.A. Quiroz, Fabrication and application of Nafion®-modified boron-doped diamond electrode as sensor for detecting caffeine, Diamond and Related Materials. 19 (2010) 1188–1193. https://doi.org/10.1016/j.diamond.2010.05.004.

[21] U. Kalsoom, A. Peristyy, P.N. Nesterenko, B. Paull, A 3D printable diamond polymer composite: a novel material for fabrication of low cost thermally conducting devices, RSC Adv. 6 (2016) 38140–38147. https://doi.org/10.1039/C6RA05261D.

[22] O. Babchenko, A. Kromka, J.P. Conde, V. Chu, T. Schmiedinger, B. Rezek, Optically transparent diamond–PDMS microfluidic system for electronic monitoring of cells, Physica Status Solidi (b). 251 (2014) 2593–2598. https://doi.org/10.1002/pssb.201451173.

[23] Q. Liang, S.A. Catledge, Y.K. Vohra, Mechanical Properties of Boron Doped Diamond Films Prepared by MPCVD, MRS Online Proceedings Library Archive. 791 (2003). https://doi.org/10.1557/PROC-791-Q8.19.

[24] X. Liu, Y.-Y. Chang, S.N. Tkachev, C.R. Bina, S.D. Jacobsen, Elastic and mechanical softening in boron-doped diamond, Scientific Reports. 7 (2017) 42921. https://doi.org/10.1038/srep42921.

[25] N. Wiora, M. Mertens, M. Mohr, K. Brühne, H.-J. Fecht, Piezoresistivity of n-type conductive ultrananocrystalline diamond, Diamond and Related Materials. 70 (2016) 145–150. https://doi.org/10.1016/j.diamond.2016.09.018.

[26] B. Fan, C.A. Rusinek, C.H. Thompson, M. Setien, Y. Guo, R. Rechenberg, Y. Gong, A.J. Weber, M.F. Becker, E. Purcell, W. Li, Flexible, diamond-based microelectrodes fabricated using the diamond growth side for neural sensing, Microsystems & Nanoengineering. 6 (2020) 1–12. https://doi.org/10.1038/s41378-020-0155-1.

[27] P. Pobedinskas, G. Degutis, W. Dexters, J. D'Haen, M.K. Van Bael, K. Haenen, Nanodiamond seeding on plasma-treated tantalum thin films and the role of surface contamination, Applied Surface Science. 538 (2021) 148016. https://doi.org/10.1016/j.apsusc.2020.148016.

[28] K. Miyata, K. Kumagai, K. Nishimura, K. Kobashi, Morphology of heavily B-doped diamond films, Journal of Materials Research. 8 (1993) 2845–2857. https://doi.org/10.1557/JMR.1993.2845.

[29] G. De Cesare, S. Salvatori, R. Vincenzoni, P. Ascarelli, E. Cappelli, F. Pinzari, F. Galluzzi, On the electrical properties of polycrystalline diamond films on silicon, Diamond and Related Materials. 4 (1995) 628–631. https://doi.org/10.1016/0925-9635(94)05294-8.

[30] C.P. Kealey, T.M. Klapötke, D.W. McComb, M.I. Robertson, J.M. Winfield, Fluorination of polycrystalline diamond filmsand powders. An investigation using FTIR spectroscopy, SEM, energy-filteredTEM, XPS and fluorine-18 radiotracer methods, J. Mater. Chem. 11 (2001) 879–886. https://doi.org/10.1039/B006800O.

[31] O.S. Elsherif, K.D. Vernon-Parry, J.H. Evans-Freeman, P.W. May, Effect of doping on electronic states in B-doped polycrystalline CVD diamond films, Semicond. Sci. Technol. 27 (2012) 065019. https://doi.org/10.1088/0268-1242/27/6/065019.

[32] E. Verveniotis, A. Kromka, M. Ledinský, B. Rezek, How nanocrystalline diamond films become charged in nanoscale, Diamond and Related Materials. 24 (2012) 39–43. https://doi.org/10.1016/j.diamond.2011.10.002.

[33] L. Ravagnan, F. Siviero, C. Lenardi, P. Piseri, E. Barborini, P. Milani, C.S. Casari, A. Li Bassi, C.E. Bottani, Cluster-Beam Deposition and in situ Characterization of Carbyne-Rich Carbon Films, Phys. Rev. Lett. 89 (2002) 285506. https://doi.org/10.1103/PhysRevLett.89.285506.

[34] L. Rezazadeh, S. Baghshahi, A.N. Golikand, Z. Hamnabard, Structure, phase formation, and wetting behavior of BaO–SiO2–B2O3 based glass–ceramics as sealants for solid oxide fuel cells, Ionics. 20 (2014) 55–64. https://doi.org/10.1007/s11581-013-0934-x.

[35] V. Mortet, Z.V. Živcová, A. Taylor, M. Davydová, O. Frank, P. Hubík, J. Lorincik, M. Aleshin, Determination of atomic boron concentration in heavily boron-doped diamond by Raman spectroscopy, Diamond and Related Materials. 93 (2019) 54–58. https://doi.org/10.1016/j.diamond.2019.01.028.

[36] V. Mortet, Z. Vlčková Živcová, A. Taylor, O. Frank, P. Hubík, D. Trémouilles, F. Jomard, J. Barjon, L. Kavan, Insight into boron-doped diamond Raman spectra characteristic features, Carbon. 115 (2017) 279–284. https://doi.org/10.1016/j.carbon.2017.01.022.

[37] J. Jiang, Y. Tzeng, Mechanisms of suppressing secondary nucleation for low-power and low-temperature microwave plasma self-bias-enhanced growth of diamond films in argon diluted methane, AIP Advances. 1 (2011) 042117. https://doi.org/10.1063/1.3656241.

[38] M. Tsigkourakos, T. Hantschel, Z. Xu, B. Douhard, J. Meersschaut, Y. Zou, K. Larsson, M. Boman, W. Vandervorst, Suppression of boron incorporation at the early growth phases of boron-doped diamond thin films, Physica Status Solidi (a). 212 (2015) 2595–2599. https://doi.org/10.1002/pssa.201532185.

[39] M. Gabrysch, S. Majdi, A. Hallén, M. Linnarsson, A. Schöner, D. Twitchen, J. Isberg, Compensation in boron-doped CVD diamond, Physica Status Solidi (a). 205 (2008) 2190–2194. https://doi.org/10.1002/pssa.200879711.

[40] J. Chevallier, B. Theys, A. Lusson, C. Grattepain, A. Deneuville, E. Gheeraert, Hydrogen-boron interactions in $p$-type diamond, Phys. Rev. B. 58 (1998) 7966–7969. https://doi.org/10.1103/PhysRevB.58.7966.

[41] K. Hirama, H. Takayanagi, S. Yamauchi, J.H. Yang, H. Kawarada, H. Umezawa, Spontaneous polarization model for surface orientation dependence of diamond hole accumulation layer and its transistor performance, Appl. Phys. Lett. 92 (2008) 112107. https://doi.org/10.1063/1.2889947.

[42] F.S. Manciu, M. Manciu, W.G. Durrer, J.G. Salazar, K.H. Lee, K.E. Bennet, A Drude model analysis of conductivity and free carriers in boron-doped diamond films and investigations of their internal stress and strain, J Mater Sci. 49 (2014) 5782–5789. https://doi.org/10.1007/s10853-014-8309-x.

[43] W.L. Wang, M.C. Polo, G. Sánchez, J. Cifre, J. Esteve, Internal stress and strain in heavily boron- doped diamond films grown by microwave plasma and hot filament chemical vapor deposition, Journal of Applied Physics. 80 (1996) 1846–1850. https://doi.org/10.1063/1.362996.

[44] J.W. Ager, M.D. Drory, Quantitative measurement of residual biaxial stress by Raman spectroscopy in diamond grown on a Ti alloy by chemical vapor deposition, Phys. Rev. B. 48 (1993) 2601–2607. https://doi.org/10.1103/PhysRevB.48.2601.

[45] H. Li, T. Zhang, L. Li, X. Lü, B. Li, Z. Jin, G. Zou, Investigation on crystalline structure, boron distribution, and residual stresses in freestanding boron-doped CVD diamond films, Journal of Crystal Growth. 312 (2010) 1986–1991. https://doi.org/10.1016/j.jcrysgro.2010.03.020.

[46] K.E. Bennet, K.H. Lee, J.R. Tomshine, E.M. Sundin, J.N. Kruchowski, W.G. Durrer, B.M. Manciu, A. Kouzani, F.S. Manciu, Raman Microscopic Analysis of Internal Stress in Boron-Doped Diamond, Materials. 8 (2015) 2782–2793. https://doi.org/10.3390/ma8052782.

[47] S.D. Janssens, S. Drijkoningen, K. Haenen, Large piezoresistive effect in surface conductive nanocrystalline diamond, Appl. Phys. Lett. 105 (2014) 101601. https://doi.org/10.1063/1.4895458.

[48] H. Li, J. Zhang, J. Chen, Z. Luo, J. Zhang, Y. Alhandarish, Q. Liu, W. Tang, L. Wang, A Supersensitive, Multidimensional Flexible Strain Gauge Sensor Based on Ag/PDMS for Human Activities Monitoring, Scientific Reports. 10 (2020) 4639. https://doi.org/10.1038/s41598-020-61658-z.

[49] M. Amjadi, A. Pichitpajongkit, S. Lee, S. Ryu, I. Park, Highly Stretchable and Sensitive Strain Sensor Based on Silver Nanowire–Elastomer Nanocomposite, ACS Nano. 8 (2014) 5154–5163. https://doi.org/10.1021/nn501204t.

[50] C.-X. Liu, J.-W. Choi, Analyzing resistance response of embedded PDMS and carbon nanotubes composite under tensile strain, Microelectronic Engineering. 117 (2014) 1–7. https://doi.org/10.1016/j.mee.2013.11.013.

[51] R. Rahimi, M. Ochoa, W. Yu, B. Ziaie, Highly Stretchable and Sensitive Unidirectional Strain Sensor via Laser Carbonization, ACS Appl. Mater. Interfaces. 7 (2015) 4463–4470. https://doi.org/10.1021/am509087u.

[52] M. Hempel, D. Nezich, J. Kong, M. Hofmann, A Novel Class of Strain Gauges Based on Layered Percolative Films of 2D Materials, (2012). https://doi.org/10.1021/nl302959a.

[53] S.-H. Bae, Y. Lee, B.K. Sharma, H.-J. Lee, J.-H. Kim, J.-H. Ahn, Graphene-based transparent strain sensor, Carbon. 51 (2013) 236–242. https://doi.org/10.1016/j.carbon.2012.08.048.

[54] J. Zhao, G. Wang, R. Yang, X. Lu, M. Cheng, C. He, G. Xie, J. Meng, D. Shi, G. Zhang, Tunable Piezoresistivity of Nanographene Films for Strain Sensing, ACS Nano. 9 (2015) 1622–1629. https://doi.org/10.1021/nn506341u.

[55] Y. Cheng, R. Wang, J. Sun, L. Gao, A Stretchable and Highly Sensitive Graphene-Based Fiber for Sensing Tensile Strain, Bending, and Torsion, Advanced Materials. 27 (2015) 7365–7371. https://doi.org/10.1002/adma.201503558.

[56] G. Cai, J. Wang, K. Qian, J. Chen, S. Li, P.S. Lee, Extremely Stretchable Strain Sensors Based on Conductive Self-Healing Dynamic Cross-Links Hydrogels for Human-Motion Detection, Advanced Science. 4 (2017) 1600190. https://doi.org/10.1002/advs.201600190.

[57] J. Chen, Q. Yu, X. Cui, M. Dong, J. Zhang, C. Wang, J. Fan, Y. Zhu, Z. Guo, An overview of stretchable strain sensors from conductive polymer nanocomposites, J. Mater. Chem. C. 7 (2019) 11710–11730. https://doi.org/10.1039/C9TC03655E.